*Journal of The Electrochemical Society*, 2026 **173** 050504

# Bilayer Electrodes to Enable Fast Charging and High Areal Capacity Na-Ion Batteries

**Galen L. V. Brown,[z] Stanislaw P. Zankowski, and Patrick S. Grant**

*University of Oxford, Department of Materials, Oxford, OX1 3PH, United Kingdom*

We present a novel bilayer architecture of a Na-ion positive electrode consisting of two sub-layers of different active materials: sodium manganese oxide ($Na_{0.7}MnO_{2+x}$, NMO) and sodium vanadium phosphate ($Na_3V_2(PO_4)_3$, NVP). The bilayer electrodes are 100 μm thick with high areal loading of ≈17 mg cm$^{-2}$. For low current densities ($<1C \equiv 45.5$ mAg$^{-1}$cm$^{-2}$) relative electrode charging capacity was not affected by bilayering, while at higher C-rates the overall charging capacity became sensitive to the relative position of NMO and NVP sub-layers. An optimum configuration of an NMO layer between the current collector and an NVP layer (CC/NMO/NVP) significantly increased overall electrode capacity during fast charging, with capacity retention ∼30% higher than the other configurations at 3C (136 mAg$^{-1}$cm$^{-2}$). The sensitivity of electrode performance to sub-layer position was attributed to the differing voltage-capacity profiles of NMO and NVP, combined with a decrease in overpotential likely due to a reduction in through-thickness Na-ion electrolyte concentration gradients. The faster charging CC/NMO/NVP arrangement showed no significant detriment in discharge behavior, and overall the electrode discharge responses were less sensitive to the spatial arrangement of active materials.

[DOI: 10.1149/1945-7111/ae482c]

Manuscript submitted November 18, 2025; revised manuscript received February 3, 2026. Published March 3, 2026.

Supplementary material for this article is available online

Global demand for energy storage solutions is growing as consumers and nations seek to reduce carbon dioxide emissions toward net-zero by mid-century.[1] As the transition away from fossil-fuel based power generation accelerates, the grid share of renewables such as solar and wind increases, and solving the intermittency issues associated with these sources becomes more pressing.[2,3] Electrochemical energy storage has a key role in mitigating differences between energy supply and demand on grids,[4] and also plays an enabling role in increasing the uptake of electric vehicles (EVs). Lithium-ion batteries (LIBs) currently dominate electrochemical energy storage applications but rely on high-criticality materials such as cobalt, nickel, lithium and graphite, causing anxiety in the sustainability and resilience of global supply chains. Due to its low abundance, high cost and toxicity, there has been effort to reduce the Co content of high energy density lithium nickel-manganese-cobalt oxide (NMC, ($LiNi_xMn_yCo_{1-x-y}O_2$)) used in LIB cathodes. For example, despite its lower energy density (∼170 mAhg$^{-1}$ rather than ∼210 mAhg$^{-1}$ for NMC[5]), the cathode active material lithium iron phosphate (LFP, $LiFePO_4$) achieved an EV market share of ∼50% in 2024, due in large part to the abundance and consequent relatively low cost of the constituent elements.[6]

For similar reasons, sodium-ion batteries (NIBs) have attracted renewed interest, having been initially dismissed commercially due to their generally lower energy densities, slower kinetics and poor cycle life.[7,8] However, with ∼1000 times greater abundance of Na than Li,[9] and less reliance on Co and Ni in favor of more abundant metals (Mn, Fe, Al) in the cathode materials, NIBs may be well-suited to alleviate some of the resource and supply chain pressures associated with LIBs.

Through the discovery and development of new Na-ion electrode materials, the gravimetric and volumetric energy density of NIBs is comparable to the LFP/graphite Li-ion chemistry,[7] and NIBs are rapidly being commercialised. The usual choice of anode material for NIBs is hard carbon, which offers a relatively high specific capacity of 250–300 mAhg$^{-1}$.[10] The capacity of the cathode, typically $<$ 200 mAhg$^{-1}$,[8] is the main limiting factor on the energy density of NIBs, and there are a plethora of cathode chemistries under commercial consideration. These principally include layered oxides (*Reliance*, India, *HiNa*, China), polyanionic (*Tiamat*, France), and prussian blue analogues (*CATL*, China). Due to the comparatively high availability of the elements for many Na-ion battery chemistries, and the lack of a clearly superior cathode material, there is a rich space for innovation in NIB cathode chemistry.

An alternative route to higher volumetric energy density at the cell level is to increase the electrode thickness. This increases the areal capacity and the relative mass and volume of the cell occupied by the energy-storing material. However, the benefit of increasing thickness is best realised at constrained, relatively low current densities, because as current density is increased, the achievable capacity reduces due to the limited mobility of Na-ions in the electrolyte that fills the tortuous electrode pore network.[11] In this scenario, increasing the current density increases the cell polarization during charge/discharge. The polarization has its origin in the evolution of through-thickness gradients in Na-ion concentration in the electrolyte, local current density and overpotential, resulting in reduced capacity and accelerated degradation.[12,13] Figure 1 is adapted from Heubner et al. (2020), who identified Li-ion concentration polarization in the electrolyte as the reason for reduced capacity at higher C-rates in Li-ion batteries.[11] Given the similarities in electrode structure and electrochemistry, diffusion-limitations are also a dominant factor for Na-ion batteries. As a result, for practical applications LIB and NIB electrode thickness is generally limited to 50–100 μm in order to avoid significant concentration gradients in the electrolyte, and thereby retain acceptable performance.[14]

The wet-slurry slot-die method (slurry casting) that dominates electrode manufacturing also inadvertently imposes practical limits on electrode thickness, because as thickness increases, the polymeric binder (up to 5 wt%) that is dissolved and then precipitates from the slurry solvent is increasingly likely to migrate toward the electrode upper free surface during electrode drying. This has the effect of blocking porosity in the upper regions of the electrode and leaving insufficient binder at the interface with the metallic foil current collector to ensure long-term adhesion.[15]

To reduce detrimental electrolyte concentration gradients and their associated polarization effects during cycling, novel electrode arrangements and manufacturing methods that enhance ionic mobility in the electrode have been investigated. Ice-templating and laser-patterning, among other examples, can create ordered through-thickness channels that lower the through-thickness tortuosity and act as low ionic resistance 'highways' for ion transport.[16–18] Other methods involve optimisation of the active particle morphology to

---

[z] E-mail: galen.brown@stx.ox.ac.uk

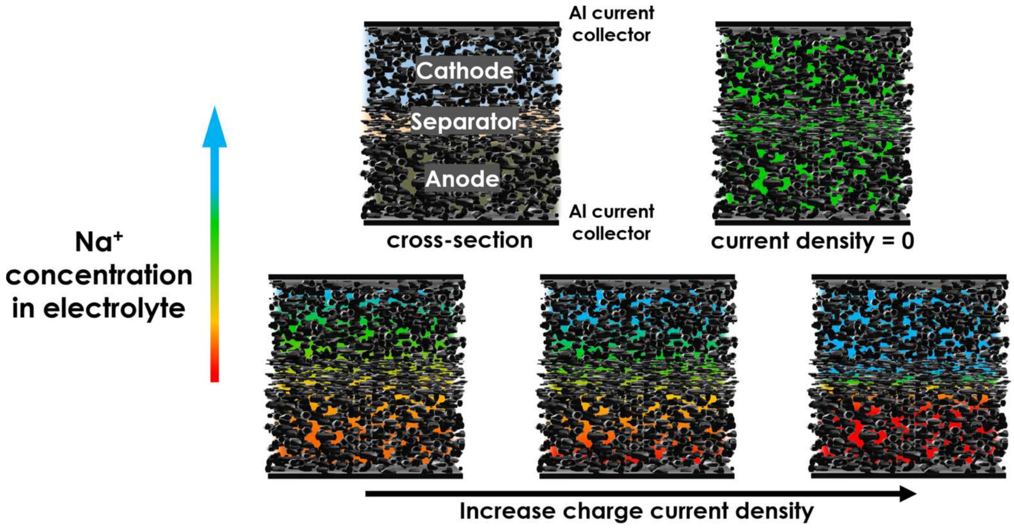

**Figure 1.** Schematic of Na-ion concentration in the electrolyte through the thickness of a sodium-ion cell at different current densities. The cell cross-section is represented as a stack of the porous cathode, separator and anode filled by electrolyte, sandwiched by Al foil current collectors. At zero current density, Na-ion concentration in the electrolyte is uniform throughout the cell. When a charging current is applied, diffusion limited transport of Na-ions results in depletion of ions in electrolyte toward the anode and enrichment toward the cathode, resulting in a concentration gradient. Further increases in current density increase the concentration gradient and lead to concentration polarization effects. The figure is adapted from Heubner et al. (2020).[11]

assist the diffusion of ions in the solid state. Additionally, there are many studies demonstrating multilayer and graded electrodes for Li-ion batteries, manufactured with deliberate through-thickness structural heterogeneity tailored to homogenize otherwise heterogeneous electrochemical conditions during charge/discharge.[16,19–21]

It is evident that, even for electrodes of identical overall composition, thickness, and active material loading, changes in the spatial arrangement or 'architecture' of materials can have large effects on overpotential and the resulting capacity retention, especially at high current densities. The arrangements include gradations in microstructural properties, such as particle size or porosity,[20,21] and in electrode composition - typically the distribution of carbon, binder or active material. Cheng et al. (2022) reported an enhancement in C-rate performance of an LIB via enrichment of conductive carbon additive close to the current collector, when compared with an equivalent uniform electrode of identical composition, thickness and porosity.[22,23] Improved electrode dynamics were attributed to a flattening of the spatial distribution of overpotential through the electrode thickness due to decreased charge-transfer resistance.[24]

Recently, Li-ion multilayer electrodes containing two distinct active materials were investigated by Tredenick et al. (2024), using sub-layers of NMC and LFP.[19] Experiments and modeling showed that the bilayer cathode with the LFP sub-layer next to the current collector (CC/LFP/NMC) was the optimal configuration of the two materials, with superior capacity retention at high C-rates to an otherwise identical CC/NMC/LFP arrangement as well as a single-layer uniform mix of the two materials. The CC/LFP/NMC cathode had a ~6% increase in charge capacity retention at 3C compared to both conventional, single-layer LFP and NMC electrodes, indicating a 'synergistic' effect when the two materials were combined in an optimal arrangement. This benefit was explained by the differences in open circuit potential (OCP) between the two materials. During charging, LFP undergoes oxidative de-lithiation at a lower potential than NMC, leading to sequential charging of the two sub-layers in a bilayer electrode. Simulations showed that this resulted in a more favorable (flatter) final Li-ion through-thickness concentration profile in the CC/LFP/NMC electrodes at the end of charging, maximizing the utilization of all the active materials.

Zhang et al. (2024) demonstrated the benefits of a thin LFP protective layer deposited on NMC. Compared to an equivalent NMC-only electrode, the additional LFP layer reduced thermal runaway risk, due to a reduction in transition metal dissolution and side reactions between the active material and the electrolyte.[25] Examples of bilayer electrodes for Na-ion batteries are more limited, although Yang et al. (2024) showed improved C-rate performance and cycle life using homogeneously mixed compositions of sodium vanadium phosphate ($Na_3V_2(PO_4)_3$) and sodium vanadium fluorophosphate ($Na_3V_2(PO_4)_2F_3$).[26] However, acquiring a mechanistic understanding of why a particular multilayer, multi-material electrode structure leads to performance benefits remains a challenge, and thus the efficient development of optimised multilayer architectures is hampered.

Here, we investigate a multi-layer, multi-material design for a Na-ion electrode to increase overall energy density at fast charging rates. The effect of the relative position of each sub-layer on electrochemical performance is considered, with particular attention given to the total charging capacity retention at high C-rates. Electrodes based on commercial active material powders of sodium manganese oxide ($Na_{0.7}MnO_{2+x}$, NMO, layered oxide) and sodium vanadium phosphate ($Na_3V_2(PO_4)_3$, NVP, polyanionic) were first considered, and as intended, showed marked differences in the shape of their capacity-voltage profiles. These differences were then used to distinguish the sequential charging/discharging of each material at low C-rate in a uniformly blended NMO+NVP composite electrode. When the same materials were assembled in bilayer configurations, the specific arrangement strongly impacted the charging performance at high C-rate, with the optimum arrangement delivering a ~30% increase in charge capacity retention at 3C (136 $mAg^{-1}cm^{-2}$). The optimum arrangement related to best matching the active material charging curve to the evolving local electrochemical conditions so that, overall, the utilization of both active materials was maximised over the charging cycle.

The bilayer cathodes were fabricated via sequential slurry casting of the two active materials. The scalability of this type of electrode structure has been demonstrated using simultaneous dual slot die coating of different slurry compositions.[27,28] Such examples have achieved distinct sub-layers of precise thickness while maintaining high line speeds. Dual slot die coating requires only minor modifications to slurry mixing and coating apparatus, while the infrastructure relating to drying, calendering, notching and cell assembly remains unchanged, supporting the plausibility of large-scale production of bilayer electrodes.

## Methods

***Cathode preparation.***—Before slurry casting, the active material and C65 powders were dried under vacuum at 120 °C overnight.

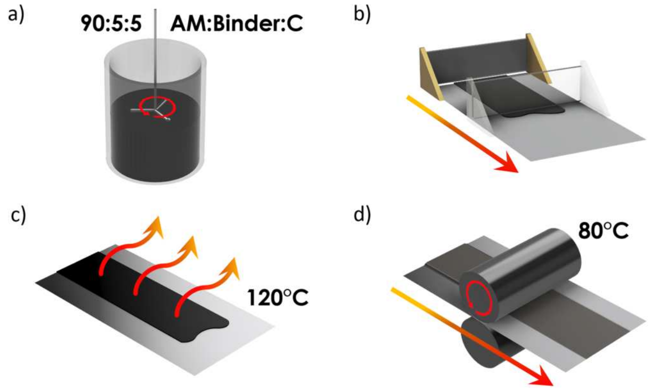

**Figure 2.** Schematic of the slurry casting method for fabrication of electrodes. **a)** Active material, PVDF binder and carbon black (90:5:5 wt %) are mixed with NMP solvent into a viscous slurry. **b)** The slurry is coated onto Al foil using a doctor blade. **c)** NMP solvent is evaporated on a hotplate and the electrode is fully dried in a vacuum oven at 120 °C. **d)** The dry electrode sheet is calendered between steel rollers held at 80 °C at constant force of 50 N/mm.

Cathodes were prepared via a slurry casting method, as illustrated in Fig. 2. Active materials, NMO (NEI, USA) or NVP (TOB, China) and carbon black (C65, Imerys, France) were mixed using an ARE-250 centrifugal planetary mixed (Thinky, Japan) with PVDF binder (Solef 5130, Solvay, Belgium) dissolved in a 3.43 wt% 1-Methyl-2-pyrrolidinone (NMP, Sigma-Aldrich) solution. The slurry was mixed in two steps: first combining the C65 and PVDF/NMP, followed by the active material, with 5 min regular mixing and 2 min de-foaming at 2000 rpm after each addition. The solid weight ratios of the materials (active material:carbon black:binder) were 90:5:5, and the solid weight content of both slurries was 40%. Slurries were cast onto Al foil (MTI) using a doctor blade and a heated draw-down table (Automatic Research, Germany) placed inside a fume hood, adjusting the blade gap to produce a coating with the target material loading of $\sim$19 mg cm$^{-2}$. The casting table was heated to 65 °C to dry the coating, followed by further drying of the electrode at 120 °C in a vacuum oven overnight.

The uniform electrodes (NMO, NVP and NMO+NVP) were cast as a single coating, dried and calendered between hot rollers held at 80 °C applying a constant force of 50 N/mm using a SUMET CA3 hot calender (Sumet Technologies GmbH *&* Co. KG, Germany), with the roller gap adjusted to produce a target electrode thickness of $\sim$100 $\mu$m and porosity of $\sim$40%. For the bilayer electrodes, the first layer was cast and dried fully, then calendered between hot rollers under the same conditions, but instead with a gap only slightly less than the dried layer thickness. Rather than significantly reducing the porosity, this intermediate calendering step ensured a smooth surface upon which the second layer of the other active material was coated and dried. After the second coating and drying steps, both NMO and NVP sub-layers in the bilayer electrode were calendered together, with the roller gap adjusted to produce the final target thickness of $\sim$100 $\mu$m and porosity of $\sim$40%.

The areal loading of the electrode sheets was measured by punching out several 14 mm electrode discs using a manual punch (Wellcos Corporation, South Korea) and measuring the active mass. The thickness of each disc after calendering was measured using a standing micrometer.

***Anode preparation.***—Hard carbon anodes were prepared using the same slurry casting method as detailed previously, but instead using carboxymethyl cellulose (CMC, molecular weight 600,000, ⩾99.5% purity, MSE Supplies, USA) and styrene-butadiene rubber (SBR, Zeon Corporation, Japan) in aqueous solution as the binder. Hard carbon powder (PI-KEM, UK) was mixed with carbon black (C65, Imerys, France) and 2 wt% CMC and 40 wt% SBR solutions in a solid wt% ratio 88:3:3:6, and then cast onto Al foil. After drying, the anode sheets were calendered to a target thickness of 75 $\mu$m and porosity of $\sim$45%. Electrode discs were punched out with a diameter of 16 mm, over-sized relative to the cathode, to ensure adequate overlap between the two electrodes after cell assembly.

***Electrode characterization.***—Electrodes for electron microscopy were prepared by cross-sectioning with a broad Ar ion-beam (PECS II, Gatan, USA) and then imaged in a scanning electron microscope (Zeiss Merlin, Germany) with a 10 kV and 2 nA beam.

The bulk electrical resistivity of single-layer and bilayer electrodes was measured using a four-point probe (Ossila, UK). For these measurements, the electrode slurry formulation was cast onto insulating polyethylene terephthalate (PET) sheet and calendered to 40.0 ± 3% porosity and 100 ± 4 $\mu$m thickness.

***Cell assembly.***—For the testing of cathodes, three-electrode PAT-cells (EL-CELL, Germany) were assembled in an Ar-filled glove box ($H_2O$ $< 0.1$ ppm, $O_2$ $< 0.1$ ppm) using a hard carbon counter-electrode, with a glass fiber separator (Whatman GF/A, 260 $\mu$m , EL-CELL) and insulation sleeve containing a metallic Na ring reference electrode). For all cells, 150 $\mu$L of 1M NaTFSI in 1:1 wt% DMC:EC electrolyte (Solvionic, France) was used.

The same procedure was used to assemble half-cells of NMO and NVP, with a metallic Na disc (⩾99.9% purity, Merck, Germany) as the counter-electrode, in order to characterize the materials at maximum capacity, given the capacity losses associated with the formation of the solid electrolyte interface (SEI) in hard carbon-based cells, as well as the incomplete sodiation of the NMO. To assess the electrochemical properties of hard carbon and to estimate the ratio of anode to cathode capacity (N/P ratio) for the full cells, three-electrode half-cells were also assembled in the same way using hard carbon as the working electrode, and Na as both counter- and reference electrodes. The electrochemical data for NMO, NVP (Fig. A.1) and hard carbon (Fig. A.2) vs. $Na^+/Na$ is shown in the supplementary data in appendix A.

***Electrochemical characterization.***—For the single-material, blended NMO+NVP and bilayer cathodes, PAT-cells were tested using a battery cycler (BioLogic VSP, France). Two formation cycles were performed at 0.05C, followed by three cycles at 0.1C. The charging C-rate was then varied by changes in the applied current density, performing five cycles each of 0.5C, 1C, 2C, and 3C, while keeping the discharge C-rate constant at 0.1C. The assumed specific capacity (by mass of active material) for the calculation of C-rate was 70.0 mAhg$^{-1}$, equivalent to a current density of 45.5 mA cm$^{-2}$g$^{-1}$. The upper and lower voltage limits were 3.6 V and 2.3 V respectively. During discharge, when the lower voltage limit was reached, the potential of the working electrode was held at 2.3 V until the current density fell to half its initial value. Before each change from a charging current density to a discharging current density (and vice versa) the cells were allowed to rest for 30 seconds. For the bilayer and NMO+NVP cathodes, the same procedure was carried out but instead varying the discharge C-rate from 0.05–0.1C to 0.5C, 1C, 2C and 3C, while keeping the charging C-rate constant at 0.1C.

For longer-term cycling, the electrodes underwent two cycles charging and discharging at 0.05C followed by one cycle at 0.1C as a formation step. The cells were then charged and discharged continuously at 1C, with a cycle at 0.3C every 20 cycles (including immediately after formation).

***Electrochemical impedance.***—Electrochemical impedance spectroscopy (EIS) measurements for NMO and NVP electrodes were also made using a battery cycler (BioLogic, France). PAT-cells were assembled in a symmetrical arrangement, using two identical electrode discs of either NMO or NVP. A non-intercalating electrolyte, comprising 10 mM tetrabutylammonium chlorate in 1:1 vol. EC:DMC, was used to prevent electrochemical reactions and impose the ‘blocking conditions’ necessary to measure the pore resistance of

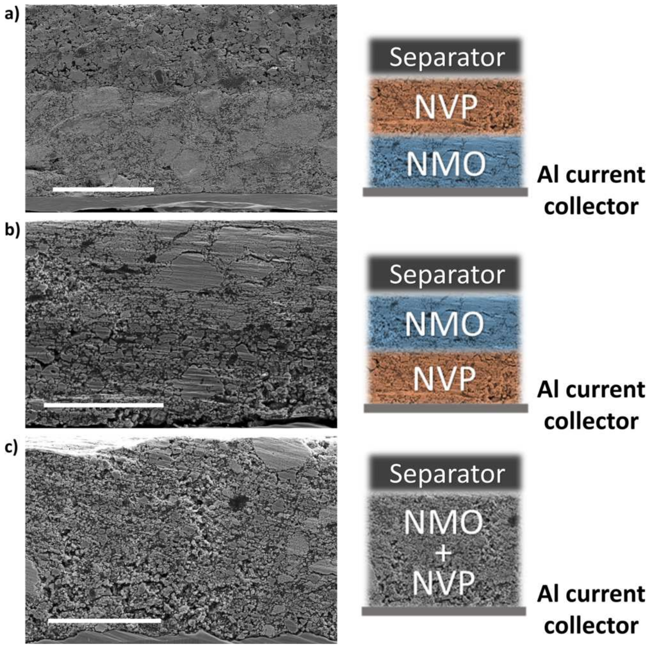

**Figure 3.** Scanning electron microscopy (SEM) images of (a) CC/NMO/NVP, (b) CC/NVP/NMO and (c) NMO+NVP arrangements. The separator depicted in corresponding schematics is not shown in the SEM images. Scale bars correspond to 50 μm.

electrodes as described by Landesfeind *et al*,[29,30]. EIS spectra were acquired setting the DC voltage to the open circuit voltage of the cells, using a voltage perturbation of 15 mV, and sweeping the frequency between $10^{-2}$–$10^{5}$ Hz.

## Results and Discussion

Scanning electron microscope (SEM) images of the three electrode types are shown in Fig. 3. Hereafter, the notation CC/NMO/NVP denotes an arrangement in which the NVP is situated on top of the NMO layer supported by the current collector (CC). For a fair comparison, we aimed to ensure that the individual layer thickness and the overall porosity of the final electrodes were the same. Due to the difference in bulk density of NMO (4.25 g cm$^{-3}$) and NVP (3.04 g cm$^{-3}$), the mass loading for each layer was different to ensure a layer thickness of 50 μm and porosity of 40%.[31,32] Figures 3a–3b show well-defined sub-layers in the CC/NMO/NVP and CC/NVP/NMO electrodes, respectively, with little intermixing of the materials at the bilayer interface. The layers were of approximately equal thickness at ~50 μm. The mixed NMO+NVP electrode in Fig. 3c had a thickness of ~100 μm, as intended. The measured average active mass loading, thickness and porosity of each type of electrode is given in Table I.

To measure the charging performance of the electrodes, after conditioning cycles at low current density (2.27–4.55 mAg$^{-1}$cm$^{-2}$) they were cycled against hard carbon anodes at increasing charging current densities of 22.7–136 mAg$^{-1}$cm$^{-2}$ (corresponding to C-rates of 0.5–3C) while keeping the same low discharge current density of 4.55 mAg$^{-1}$cm$^{-2}$ (0.1C). Rather than varying the current density according to the measured capacity of each electrode, the same current densities were applied to all electrodes, based on 1C = 70.0 mAg$^{-1}$ at an active mass of 45.5 mAg$^{-1}$cm$^{-2}$. For each charging C-rate, five charge-discharge cycles were applied and the capacities averaged.

Figure 4a shows the absolute charge capacities of the three composite electrodes at increasing charging current density. At low C-rates of 0.05–0.1C, the mixed NMO+NVP electrode had a capacity of 72.0 ± 0.3 mAhg$^{-1}$, which was ~20% higher than the bilayered CC/NMO/NVP (58.0 ± 2 mAh g$^{-1}$) and CC/NVP/NMO (52.9 ± 0.9 mAhg$^{-1}$) electrodes. The differences can be understood by considering the charging of the single-layered NMO and NVP electrodes with capacities of 34.6 ± 8 mAhg$^{-1}$ and 91.7 ± 1.2 mAhg$^{-1}$, respectively (Supplementary Fig. A.3). The NMO ($Na_{0.7}MnO_{2+x}$) was provided partially sodiated, and (i) assuming the Na content of the NMO could not exceed 0.7 per formula unit and (ii) a minimum Na content of ~0.4 according to the voltage range of 2.3–3.6 V, then the calculated capacity of NMO was ~73 mAhg$^{-1}$.[33] For NVP, assuming the reversible intercalation of 2 Na ions per formula unit, the calculated capacity was 118 mAhg$^{-1}$.[34] Figure 4a shows both NMO and NVP had a capacity lower than calculated, which was attributed to Na loss due to SEI layer formation on the hard carbon counter-electrode.[35] In addition, for the various two-material electrodes, because the NMO and NVP have different densities and capacities, using constant thickness electrodes makes comparing the different electrode absolute capacities complex. To account for this, the relative change in capacity of each electrode with charging C-rate was considered a more intuitive way of comparing performance. The relative capacities were calculated as the retained capacity as a fraction of the average capacity measured during cell pre-conditioning at very low current density (0.05–0.1C).

**Table I. Properties of the bilayer, mixed and single-material electrodes based on NMO and NVP. The uncertainties are the calculated standard deviation for each electrode type. For calculation of the porosity, the relative quantity of each active material was considered, together with the respective bulk densities of NMO and NVP and the other solid components.**[31,32]

| Electrode type | Active mass (mg cm$^{-2}$) | Thickness (μm) | Porosity (%) |
|---|---|---|---|
| NMO | 21.1 ± 0.5 | 100 ± 2 | 37.4 ± 1.3 |
| NVP | 16.2 ± 0.7 | 96.1 ± 3 | 34.0 ± 3 |
| NMO+NVP | 17.5 ± 0.3 | 101 ± 4 | 40.0 ± 1.1 |
| CC/NMO/NVP | 16.7 ± 0.6 | 99.0 ± 4 | 40.1 ± 2 |
| CC/NVP/NMO | 17.2 ± 0.3 | 101 ± 4 | 39.7 ± 0.9 |

Figure 4b shows that when charged at C-rates up to 1C, the bilayer and mixed electrodes showed similar capacity retention, but then significantly diverged at 2C and 3C. Both the mixed and CC/NVP/NMO electrodes displayed the typical shape for diffusion-limited charging (strongly decreasing capacities at higher C-rates).[11] On the other hand, the capacity of CC/NMO/NVP electrodes varied only slightly over the range, e.g. at 3C (charging current density of 136 mAg$^{-1}$cm$^{-2}$), the CC/NMO/NVP arrangement had a capacity retention of 67.1 ± 4% - only ~20% lower than the retention at 0.5C, but nearly double the 3C retention of CC/NVP/NMO (36.4 ± 12%) and NMO+NVP (33.1 ± 9%). Notably, the absolute capacity of the CC/NVP/NMO electrode at 3C surpassed that of the NMO+NVP electrode, despite the larger content of high-capacity NVP in the latter electrode, and that the NMO in the bilayer was subject to a C-rate closer to 4C than 3C due to its lower intrinsic capacity. At the highest charging current densities, the capacity retention of the optimal bilayer configuration exceeded that of the single-layer NVP (57.2 ± 3%) and single-layer NMO (35.8 ± 2%) electrodes, as shown in Fig. A.3 (although the absolute capacity of the NVP-only electrodes remained higher at all C-rates).

Figure 5 shows representative potential-capacity plots at different charging C-rates for each type of electrode. The profile of single-layered NMO electrode in Fig. 5a had a slanting potential between 2.3 and 3.6 V, characteristic of the NMO de-sodiation reaction via a mostly solid-solution mechanism with a lack of distinctive phase transitions,[33,36] given by:

$$Na_{0.7}MnO_{2+x} \rightleftharpoons Na_{0.4}MnO_{2+x} + 0.3Na^{+} + 0.3e^{-} \qquad [1]$$

In contrast, the profile of single-layered NVP electrode in Fig. 5b shows a plateau at 3.4 V due to the de-intercalation of 2 Na ions per formula unit of NVP via a phase-change mechanism according to:[34]

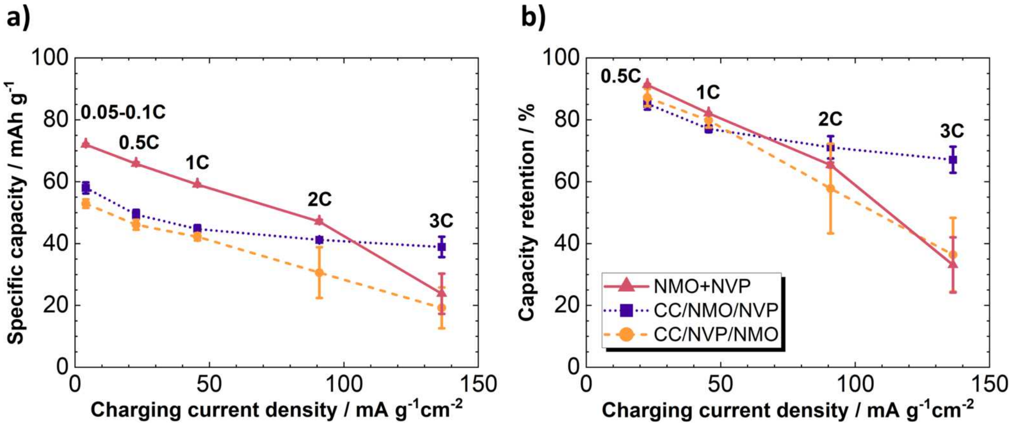

**Figure 4.** Comparison of C-rate performance of the two bilayered electrodes, CC/NMO/NVP and CC/NVP/NMO, and the NMO+NVP mixture. The voltage range was 2.3–3.6 V. (**a**) Absolute specific capacity vs. current density, equivalent to defined C-rates of 0.05-0.1C, 0.5C, 1C, 2C and 3C. (**b**) Capacity retention (as a fraction of average capacity during cell pre-conditioning at 0.05-0.1C) with respect to current density. Here 1C ≡ 70.0 mAg$^{-1}$ of active material and 45.5 mAg$^{-1}$cm$^{-2}$ of electrode surface area. All capacities are referenced to the geometrical area of the electrodes and summed mass of active materials in the electrodes. Data is averaged over at least three cells of each type, with error bars indicating the standard deviation.

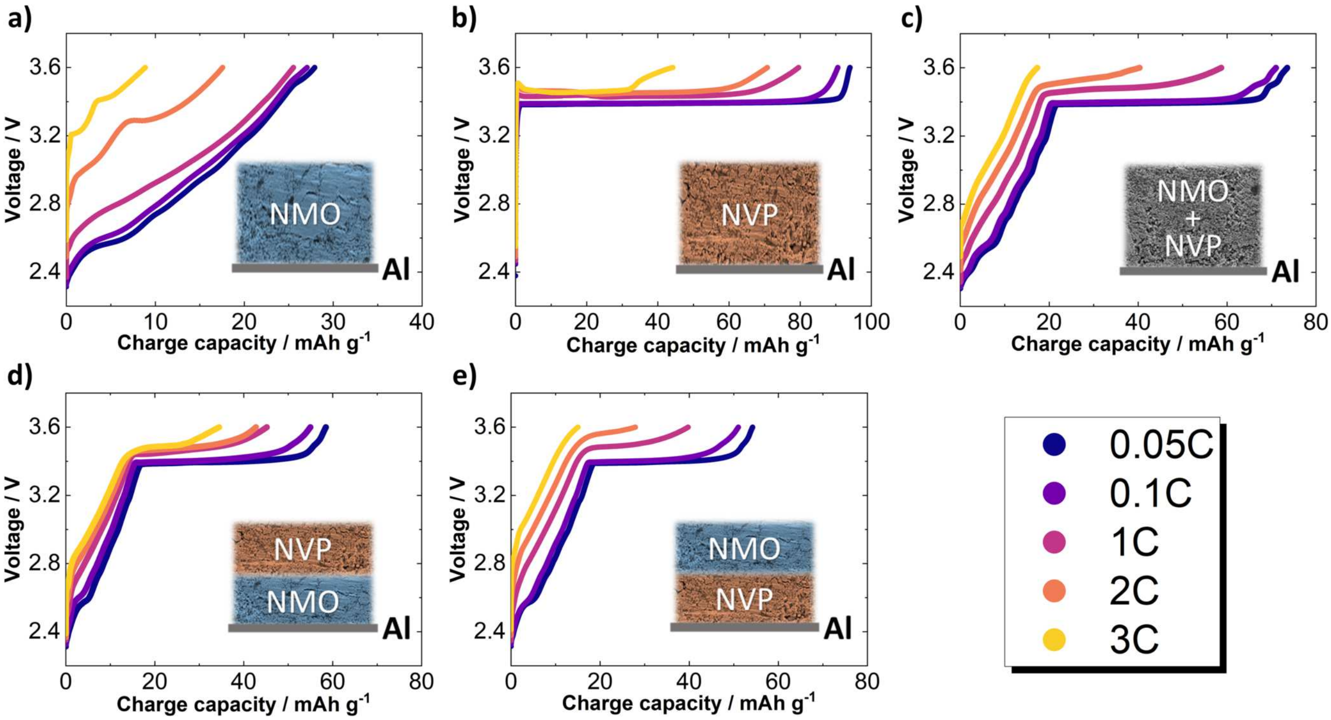

**Figure 5.** Charging profiles of **a)** NMO, **b)** NVP, **c)** NMO+NVP, **d)** CC/NMO/NVP and **e)** CC/NVP/NMO electrodes at C-rates of 0.1C, 0.5C, 1C, 2C and 3C vs. a hard carbon counter-electrode. For all electrodes, the voltage window was 2.3–3.6 V, with $1C \equiv 45.5$ mAg$^{-1}$cm$^{-2}$.

$$\mathrm{Na_3V_2(PO_4)_3 \rightleftharpoons NaV_2(PO_4)_3 + 2Na^+ + 2e^-} \quad [2]$$

While the NMO plot shifted to higher potential with increasing C-rate, the NVP plateau was only slightly shifted, suggesting a lower overall electrode resistance.

Figure 5c shows similar profiles for a mixed NVP+NMO electrode, where sequential charging of NMO (slanting potential region up to 3.4 V), followed by charging of NVP (plateau region at 3.4 V) was evident at low C-rates. The same behavior was also shown in the low C-rate profiles of CC/NMO/NVP and CC/NVP/NMO electrodes in Figs. 5d and 5e, respectively. While the voltage profiles for the composite electrodes were generally similar with an NMO relative contribution to capacity of ~20 mAhg$^{-1}$, there were significant differences in the absolute contribution of the NVP to capacity in the mixed and bilayered electrodes. In NVP+NMO, the 3.4 V plateau contributed 47 mAhg$^{-1}$ of capacity compared with 37 mAhg$^{-1}$ in CC/NMO/NVP and 30 mAhg$^{-1}$ for CC/NVP/NMO, due to larger relative content of the higher capacity NVP in the NVP+NMO electrode compared with the bilayer electrodes, as explained previously. Qualitatively, in the two-material electrodes at low C rates there was sequential charging of NMO followed by NVP, independent of the position of each active material in the electrode, because at low current densities, the mobility of Na-ions through the electrolyte is not a limitation, and active materials could deliver the same relative capacity regardless of their location.

During charging at higher C-rates, however, there were clear differences in the behavior of the electrodes. In the NVP+NMO and CC/NVP/NMO electrodes, there was an increase in potential of NMO charging, along with a gradual reduction and eventual disappearance of the NVP capacity contribution at 3C. Conversely in the CC/NMO/NVP electrodes, the NMO potential increases were significantly lower, and even at 3C, ∼50% of the low C-rate capacity of NVP contributed to overall capacity. Comparison of Figs. 5d–5e show that the optimum CC/NMO/NVP arrangement had a decisive role in increasing overall active materials utilization.

To explore this behavior further, Fig. 6 plots the overpotential applied to each cathode (as measured in the three-electrode PAT-cell) as a function of C-rate. Following[12] we estimated the overpotential as the difference in the measured cell potential to the charging potential recorded during cell pre-conditioning at 0.05-0.1C, which approximated to the electrode open circuit potential (OCP). For the single material electrodes in Figs. 6a–6b, NMO charging required higher overpotentials than NVP, and overpotential increased more steeply as C-rate increased (e.g. at 3C, 850 mV for NMO compared with 100 mV for NVP). In the case of electrodes containing both NMO and NVP, similarly to the C-V curves in Fig. 5, the charging behavior of the two materials could again be clearly differentiated. The lowest NMO overpotential was exhibited by the CC/NMO/NVP electrode, consistent with its superior capacity, despite the NMO being positioned furthest from the separator. For CC/NVP/NMO, where the NMO layer was now close to the separator, the peak overpotential increased by ∼200 mV.

To further elucidate the differences in performance of the bilayer cathodes, the separate influences of electronic and ionic resistance were investigated. The bulk electrical resistivity of each electrode type was quantified using a four-point probe, as shown in Table II. For the single-material electrodes, NVP had a significantly lower electrical resistivity than NMO, at 29.7 ± 1.7 mΩ m compared with 44.3 ± 5 mΩ m. This partially explains the superior capacity retention at higher C-rates of NVP relative to NMO, as capacity is sensitive to resistance to electron flow through the solid electrode to the current collector. For the electrodes containing both active materials, the electrical resistivity was sensibly between the NMO and NVP alone. The relative position of the NMO and NVP in the electrodes had no significant effect on bulk resistivity. The slightly lower average resistivity of NMO+NVP than the bilayer was attributed to the greater fraction of NVP. Overall, the differences in bulk electrical resistivity were not considered significant in controlling the differing electrochemical behavior of the composite electrodes.

The impedance spectra of NMO and NVP electrodes at a full state of charge were measured using symmetrical, three-electrode cells with a non-intercalating electrolyte, and the resulting Nyquist plots are shown in Fig. 7. As described by Landesfeind et al. (2017), under these 'blocking conditions', the electrode contact resistance and pore ionic resistance can be resolved.[30] The former arises from the electronic resistance between the electrode layer and the current collector, while the latter relates to the ionic resistance of Na ion transport through the tortuous interconnected pore network. The data were best-fitted to give estimates for the contact resistance $R_{Contact}$ (visually represented by the diameter of the high-frequency semicircle) of 36.1 ± 3 Ω and 22.8 ± 8 Ω for NMO and NVP respectively. From linear fitting of the low-frequency domain, and by subtraction of the contact resistance and high-frequency resistances ($R_{hf}$), pore ionic resistance ($R_{Pore}$) was estimated as 107 ± 20 Ω and 79.9 ± 17 Ω for NMO and NVP respectively.[37]

The higher contact resistance for NMO was likely influenced by its higher electronic resistivity and a less intimate current collector-electrode interface due to particle agglomeration (Fig. 3). Despite the similar bulk electrical resistivity of the bilayer cathodes, the higher resistance at the current collector can be expected to be detrimental to the CC/NMO/NVP electrode relative to the CC/NVP/NMO. But, this is in contrast to the better charging performance of CC/NMO/NVP. Furthermore, the lower electronic resistivity of the NVP electrodes over NMO might also be expected to favor the CC/NVP/NMO arrangement, as reduced electronic resistivity in the region nearest the current collector is known to be beneficial to rate performance.[23] But again, the charging response of the CC/NMO/NVP was the best of all arrangements, suggesting that electronic effects were not the decisive factor in its superior performance.

Instead, ionic resistance may have played a larger role, given that pore resistivity, $\rho_{Pore}$, for both NMO and NVP was ∼4000 times greater than the electrical resistivity as shown in Table II. Together

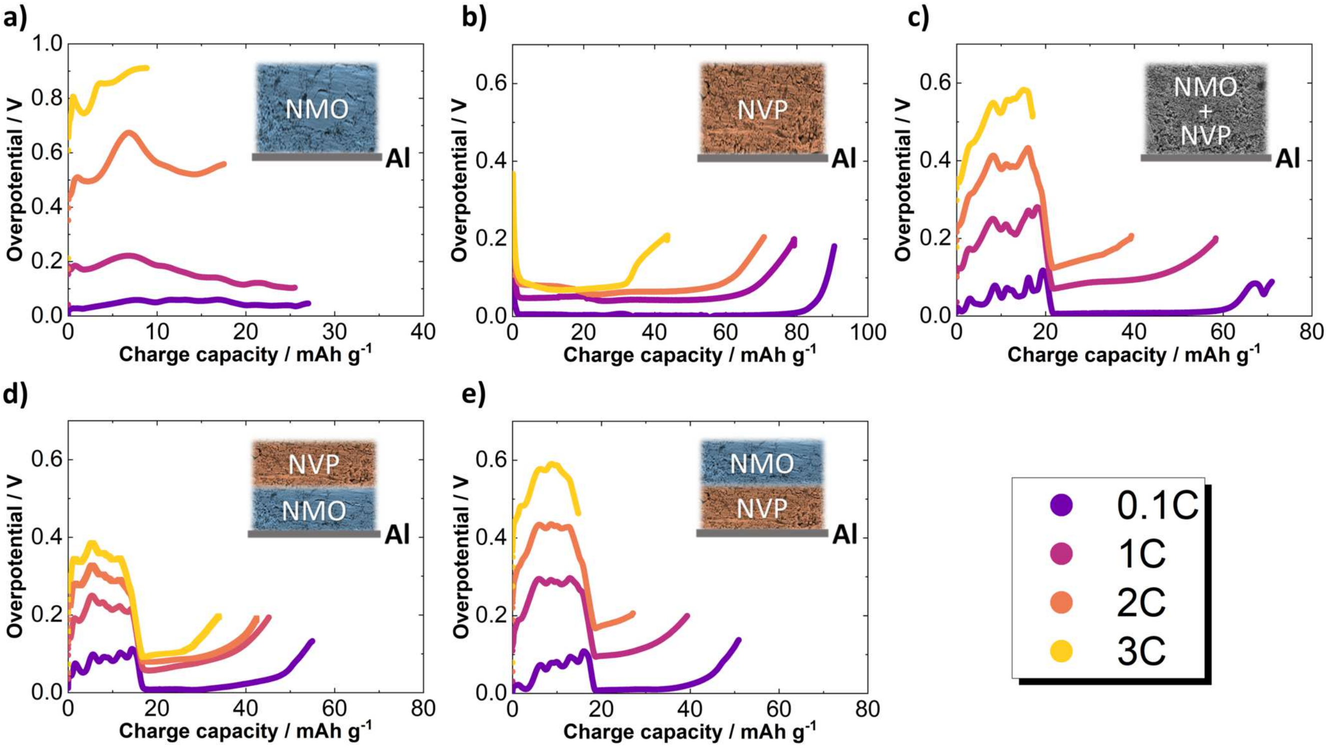

**Figure 6.** Overpotential measured as a function of charge capacity for **a)** NMO, **b)** NVP, **c)** NMO+NVP, **d)** CC/NMO/NVP and **e)** CC/NVP/NMO electrodes at C-rates of 0.1C, 1C, 2C and 3C (blue, green, orange and red respectively) vs. a hard carbon counter-electrode. For all electrodes, the voltage window was 2.3-3.6 V, with $1C \equiv 45.5\ \mathrm{mAg^{-1}cm^{-2}}$. Overpotential was estimated by subtracting the C-V curves for each C-rate from that measured at 0.05C.

**Table II. Electronic and ionic resistances of electrodes. Shown are bulk electrical resistivity ($\rho_{El}$) and resistance ($R_{El}$) for the bilayer, mixed and single-material electrodes based on NMO and NVP. Also included is the contact resistance ($R_{Contact}$), pore ionic resistivity ($\rho_{Pore}$) and pore ionic resistance ($R_{Pore}$) of the single-material electrodes. Electrical resistivity was measured using a four-point probe, while the contact and pore ionic resistances were calculated from the impedance spectra as shown in Fig. 7. All resistances were calculated for circular electrodes with 14 mm diameter. The uncertainties are the standard deviation in the measurements for each electrode type.**

| Electrode type | $\rho_{El}$ (mΩ m) | $R_{El}$ (mΩ) | $R_{Contact}$ (Ω) | $\rho_{Pore}$ (Ω m) | $R_{Pore}$ (Ω) |
|---|---|---|---|---|---|
| NMO | 44.3 ± 5 | 28.8 ± 3 | 36.1 ± 3 | 153 ± 30 | 107 ± 20 |
| NVP | 29.7 ± 1.7 | 19.3 ± 1.1 | 22.8 ± 8 | 124 ± 30 | 79.9 ± 17 |
| NMO+NVP | 37.1 ± 4 | 24.1 ± 3 | — | — | — |
| CC/NMO/NVP | 39.5 ± 1.2 | 25.7 ± 0.8 | — | — | — |
| CC/NVP/NMO | 41.8 ± 4 | 27.2 ± 3 | — | — | — |

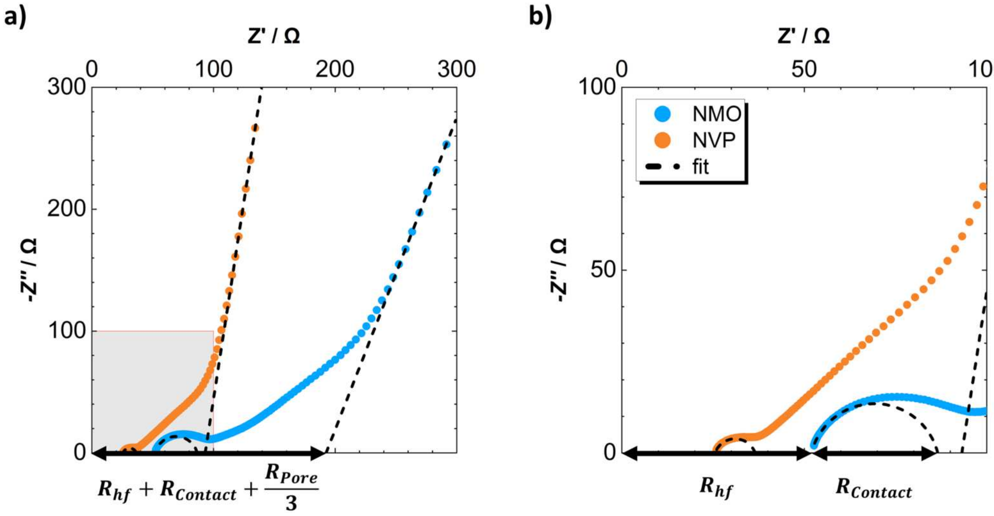

**Figure 7.** Electrochemical impedance spectra (EIS) of NMO and NVP electrodes. **a)** The full impedance spectra, with best fits for the semicircular and linear domains. Labelled for NMO is the sum of high-frequency ($R_{hf}$), contact ($R_{Contact}$) and pore ($R_{Pore}$) resistances which form the real axis intercept of the linear fit. **b)** Enlarged high-frequency domain of the EIS spectrum. Labelled for NMO are the high-frequency and contact resistances, measured respectively as the real axis offset and diameter of the semicircular fit. Each type of electrode was characterised using a symmetrical three-electrode setup (metallic Na reference) with a non-intercalating electrolyte (10 mM tetrabutylammonium chloride in 1:1 vol. EC:DMC). EIS measurements were performed in potentiostatic mode, using a 10 mV perturbation and frequency range $10^{-2}$–$10^{5}$ Hz.

with estimates of electrode porosity from mass and thickness measurements, pore resistance was used to estimate the tortuosity factor $\tau$:

$$\tau = \frac{R_{Pore}A\kappa}{d}\epsilon \qquad [3]$$

where A is the cross-sectional area of the electrode, $\kappa$ is the ionic conductivity of the electrolyte, d is the electrode thickness and $\epsilon$ is the porosity.[29] Because the electrolyte ionic conductivity was the same for both electrodes, Eq. 3 could be simplified to give a tortuosity ratio of NMO and NVP of $\tau_{NMO}/\tau_{NVP} = 1.42 \pm 0.4$, taking into account the uncertainty in the thickness and porosity measurements.

The ~40% higher tortuosity of the NMO electrode compared with the NVP electrode might arise from the higher propensity for agglomeration of the NMO active particles, as also evident in the SEM images in Fig. 3. The comparatively lower tortuosity of the NVP layer should be beneficial to the CC/NMO/NVP arrangement, because the low tortuosity of the upper NVP sub-layer facilitates access of the $Na^+$ ions into the deeper parts of the electrode and improves its overall rate performance.[20,38] This may partially explain why the CC/NMO/NVP electrode performed better - despite the higher contact resistance of NMO.

Even accounting for these factors, the superior rate performance of the CC/NMO/NVP electrode was primarily attributed to the lower de-sodiation potential of NMO compared to NVP, as seen in the charging profiles of Figs. 5a–5b. Placing NMO closer to the current collector reduces Na-ion concentration polarization effects (as seen on the overpotential plots in Fig. 6), the implication of which is that more uniform through-thickness charging is promoted. This interpretation is consistent with the findings of Tredenick et al. (2024) who found the optimal arrangement of LFP and NMC-622 in a bilayer Li-ion electrode to be CC/LFP/NMC, attributed primarily to the lower de-lithiation potential of LFP and verified using a multilayer Doyle-Fuller-Newman model.[19] Following the same reasoning, the reverse electrode configuration (CC/NVP/NMO) gives the least charging capacity, because a higher charging overpotential developed as the sluggish Na transport from the NVP layer (away from the separator) was amplified by the high de-sodiation potential of NVP. The similarity of NMO and NVP bilayer behavior to other bilayer combinations such as NMC and LFP, noting that within these Li and Na cathode systems the bilayers have qualitatively similar open circuit voltage profiles, gives confidence in the general, wider applicability of the bilayer concept. Confidence is further boosted by modelling of a Li-ion bilayer that provided further insight into the factors determining an optimal sub-layer arrangement, and can be a predictive tool for more efficient bilayer electrode design.[19,39]

Finally, the same cycling procedure was applied to bilayer and blended NMO+NVP cathodes, but instead varying the discharge C-rate (0.5C, 1C, 2C, 3C) while keeping the charge rate constant at 0.1C, and again assuming a specific capacity of 70.0 $mAhg^{-1} = 45.5$ $mAhg^{-1}cm^{-2}$ for defining C-rate. Figures 8a–8b show the average electrode absolute and relative capacities. Similarly to the charging capacities, the absolute discharge capacities of NMO+NVP were larger than the bilayered electrodes due to the higher relative content of the higher capacity NVP. Furthermore, as with charging, the discharge capacity retention of all electrodes was similar at low C-rates, but diverged increasingly up to 3C. However, the differences in capacity retention were smaller, with CC/NMO/NVP and NMO+NVP having a similar 3C discharge capacity retention of 66.5 ± 2% and 64.2 ± 6% respectively. Meanwhile, CC/NVP/NMO performed significantly worse, with a 3C capacity retention of 48.1 ± 4%.

Figures 8c–e and 8f–h show the capacity-voltage and overpotential plots of the electrodes during discharge, respectively. For all electrodes, the separated and sequential discharge of NVP followed by NMO was observed for 0.05C-0.1C, but as C-rate was increased, their distinct contributions became harder to differentiate. As seen in Fig. 8h, the CC/NVP/NMO showed the most rapid increase in overpotential at 2C and 3C, supporting the assertion that layering of the NVP furthest from the separator undermined its capacity contribution. The optimal CC/NMO/NVP arrangement for charging had a lower overpotential at the start of discharge at all C-rates (Figs. 8d and 8g), which allowed for a greater utilization of NVP due to its favorable position next to the separator. However, this was not reflected in a higher overall absolute capacity relative to the homogeneous NMO+NVP mixture at 3C (as was the case during charging). Overall, the discharge capacity at high C-rates was less sensitive to the spatial arrangement of the active materials than for charging.

This somewhat surprising result was also observed by Tredenick et al. in the bilayer CC/LFP/NMC electrode, which showed that the rank order of electrode performance with respect to sub-layer position for charging was not simply inverted when discharging.[19] Such asymmetric charge/discharge performance of the bilayered electrodes could relate to the different proximity of the (de)-sodiation potentials of NVP and NMO to the imposed potential cut-offs during cycling, as a result of their different energy storage mechanisms. For NVP, there is a little variation of electrochemical potential throughout the phase-change reaction. Consequently, during charging, the 3.4 V plateau of high-capacity NVP was close to the cell cutoff potential of 3.6 V, which meant the attainable capacities during charging became very sensitive to the overpotential of the cell. For the CC/NVP/NMO and NMO+NVP electrodes, large overpotentials had to be applied to sustain high current charging, and the cutoff was reached too soon before any significant capacity contribution from NVP could be realised (see Fig. 5). The optimal CC/NMO/NVP bilayered configuration exhibited the lowest overpotential during charging, and therefore delayed reaching the cutoff voltage, greatly enhancing the capacity retention. Conversely, during

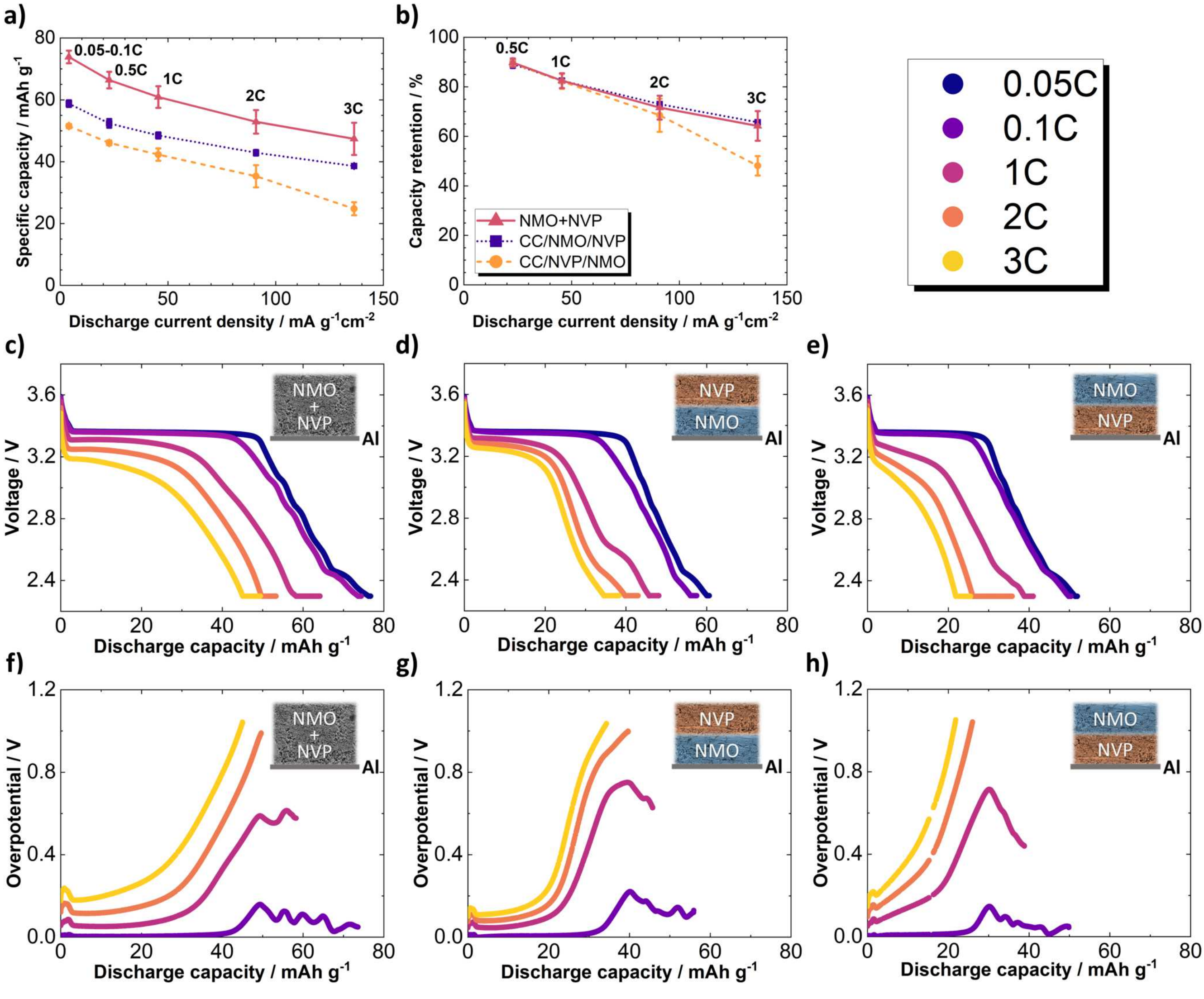

**Figure 8.** Average discharge capacity in terms of **(a)** absolute specific capacity and **(b)** capacity retention relative to that measured at 0.05-0.1C. Averages are calculated from three cells of each type, with error bars indicating the standard deviation. Also shown are capacity-voltage and corresponding overpotential profiles for individual electrodes of **(c,f)** NMO+NVP, **(d,g)** CC/NMO/NVP and **(e,h)** CC/NVP/NMO cathodes at C-rates of 0.05C, 0.1C, 0.5C, 1C, 2C and 3C vs. a hard carbon counter-electrode. For all electrodes, the voltage window was 2.3–3.6 V, with $1C \equiv 45.5$ mAg$^{-1}$cm$^{-2}$.

discharge, the NVP sodiation plateau was far from the lower cutoff of 2.3 V, allowing for better utilization before premature cutoff, even under higher overpotentials. Also, during discharge, because the sodiation of NMO occurs over an extended, slanting potential range, some of its capacity could be still accessible under relatively large overpotentials.

Overall, the superior performance of the CC/NMO/NVP cathode was principally in fast charging at ⩾2C. This was further reinforced by longer-term cycling of the composite electrodes, the first 30 cycles of which are shown in Fig. A.4. Initially, the capacity of the three electrode types at 1C was similar, with the NMO+NVP electrode having a slightly higher capacity due to its higher NVP fraction. There was no significant difference in retained capacity between the two 0.3C charge cycles (separated by 19 cycles at 1C), which for NMO+NVP, CC/NMO/NVP and CC/NVP/NMO electrodes was 90.1 ± 1.2%, 90.0 ± 3% and 92.3 ± 1.6% respectively. It is only when charging at higher current densities, where cell polarization and overpotential were more significant, that the sensitivity to sub-layer position was manifest. Nevertheless, given the limited cycling range of these tests (∼30 cycles) due to premature Na plating in all electrode types, further testing over hundreds of cycles will be needed to fully elucidate any difference in long-term stability.

## Conclusions

Relatively thick (100 μm), high-loading (17 mgcm$^{-2}$) bilayer Na-ion cathodes using NMO and NVP active materials were fabricated and characterised. Compared with homogeneously mixed composite and single-material electrodes of equivalent thickness and porosity, a CC/NMO/NVP bilayer arrangement showed significantly improved capacity retention charging at 3C (136 mAg$^{-1}$cm$^{-2}$). The improvement in retention was attributed primarily to the lower de-sodiation potential of NMO compared to NVP, mitigating the increase in cell polarization and overpotential due to buildup of concentration gradients as current density was increased. This effect relegated the benefits of the lower electrical resistivity and lower contact resistance of the NVP layer to a second order effect. In discharge behavior, structural arrangements had less influence on overall electrode response, with both CC/NMO/NVP and blended NVP+NMO electrodes showing similar relative capacity retention.

While the performance benefits of the CC/NMO/NVP cathode were only significant when charging at high current densities, at the lower C-rates the single-layer NVP and NMO+NVP showed higher gravimetric and areal capacity. Notably, the NVP electrode had a higher absolute capacity than the CC/NMO/NVP at all C-rates, despite the superior fractional capacity retention of the bilayer. This indicates, particularly for combinations such as NMO and NVP where the specific capacities of the materials differ substantially, the use of bilayer electrodes may be most suited to fast charging applications. In commercial cells with fast charging capability, such as ultra-fast charging for EVs (⩾150 kW[6]), the benefits of lower overpotential and higher capacity retention of a bilayer electrode when charging at ⩾2C may outweigh the reduction in the maximum areal capacity compared with a conventional single-layer electrode.

Microstructural differences between the sub-layers, such as particle size and tortuosity, were important to consider in understanding differences in electrode response to an increasing charging current density. Understanding how these properties interact in a bilayer electrode to influence final rate performance may allow synergistic combinations of electrode materials to be explored, whereby overall electrode dynamics are significantly superior to the performance of the component materials in a conventional single-material electrode.

## Acknowledgments

This work was supported by the UK Engineering and Physical Sciences Research Council (EPSRC) in partnership with Shell Global Solutions International B.V. via an ICASE studentship (UKRI project reference: 2740764). We would also like to thank the David Cockayne Centre for Electron Microscopy for providing training and use of the SEM facilities.

## ORCID

Galen L. V. Brown https://orcid.org/0009-0003-6707-5015
Stanislaw P. Zankowski https://orcid.org/0000-0001-8616-1849
Patrick S. Grant https://orcid.org/0000-0002-7942-7837

## References

1. V. Masson-Delmotte et al., *Global warming of 1.5°C*, Intergovernmental Panel on Climate Change (IPCC) (2019), United Nations Digital Library https://digitallibrary.un.org/record/3893415?ln=en&v=pdf.
2. J. Yin, A. Molini, and A. Porporato, "Impacts of solar intermittency on future photovoltaic reliability." *Nat. Commun.*, **11**, 4781 (2020).
3. M. Albadi and E. El-Saadany, "Overview of wind power intermittency impacts on power systems." *Electric Power Systems Research*, **80**, 627 (2010).
4. N. Kittner, F. Lill, and D. M. Kammen, "Energy storage deployment and innovation for the clean energy transition." *Nat. Energy*, **2**, 17125 (2017).
5. K. W. Knehr, J. J. Kubal, P. A. Nelson, and S. Ahmed, *Battery performance and cost modeling for electric-drive vehicles, a manual for BatPaC v5.0*, Argonne National Laboratory (2022), OSTI ID 1877590.
6. *Global EV Outlook 2025*, IEA, Paris (2025), https://www.iea.org/reports/global-ev-outlook-2025, Licence: CC BY 4.0.
7. J. Frith, M. Lacey, and U. Ulissi, "A non-academic perspective on the future of lithium-based batteries." *Nat. Commun.*, **14**, 420 (2023).
8. N. Tapia-Ruiz et al., "2021 roadmap for sodium-ion batteries." *J. Phys.: Energy*, **3**, 031503 (2021).
9. W. Zhang, F. Zhang, F. Ming, and H. N. Alshareef, "Sodium-ion battery anodes: Status and future trends." *EnergyChem*, **1**, 100012 (2019).
10. A. Bauer, J. Song, S. Vail, W. Pan, J. Barker, and Y. Lu, "The scale-up and commercialization of nonaqueous Na-ion battery technologies." *Adv. Energy Mater.*, **8**, 1702869 (2018).
11. C. Heubner, M. Schneider, and A. Michaelis, "Diffusion-limited c-rate: A fundamental principle quantifying the intrinsic limits of Li-ion batteries." *Adv. Energy Mater.*, **10**, 1902523 (2020).
12. Z. Chen, D. L. Danilov, L. H. Raijmakers, K. Chayambuka, M. Jiang, L. Zhou, J. Zhou, R.-A. Eichel, and P. H. Notten, "Overpotential analysis of graphite-based Li-ion batteries seen from a porous electrode modeling perspective." *Journal of Power Sources*, **509**, 230345 (2021).
13. W. A. Appiah, L. H. Rieger, E. Flores, T. Vegge, and A. Bhowmik, "Unravelling degradation mechanisms and overpotential sources in aged and non-aged batteries: a non-invasive diagnosis." *Journal of Energy Storage*, **84**, 111000 (2024).
14. R. E. Ciez and J. Whitacre, "Comparison between cylindrical and prismatic lithium-ion cell costs using a process based cost model." *Journal of Power Sources*, **340**, 273 (2017).
15. S. Jaiser, M. Müller, M. Baunach, W. Bauer, P. Scharfer, and W. Schabel, "Investigation of film solidification and binder migration during drying of Li-ion battery anodes." *Journal of Power Sources*, **318**, 210 (2016).
16. G. Polizos, S. Kalnaus, X. C. Chen, M. Dixit, M. Balasubramanian, J. Sharma, R. Tao, and J. Li, "Two-layer cathode architecture for high-energy density and high-power density solid state batteries." *Materials Today Chemistry*, **33**, 101704 (2023).
17. W. Pfleging, "Recent progress in laser texturing of battery materials: a review of tuning electrochemical performances, related material development, and prospects for large-scale manufacturing." *International Journal of Extreme Manufacturing*, **3**, 012002 (2021).
18. Y. Chen, B. Zhao, Y. Yang, and A. Cao, "Toward high-areal-capacity electrodes for lithium and sodium ion batteries." *Adv. Energy Mater.*, **12**, 2201834 (2022).
19. E. C. Tredenick, S. Wheeler, R. Drummond, Y. Sun, S. R. Duncan, and P. S. Grant, "A multilayer Doyle-Fuller-Newman model to optimise the rate performance of bilayer cathodes in Li-ion batteries." *J. Electrochem. Soc.*, **171**, 060531 (2024).
20. R. Chowdhury, Y. Zhao, Y. Xia, M. Ouyang, N. Brandon, and A. Banerjee, "Revisiting the promise of bi-layer graded cathodes for improved Li-ion battery performance." *Sustainable Energy Fuels*, **5**, 5193 (2021).
21. M. Wood, J. Li, Z. Du, C. Daniel, A. R. Dunlop, B. J. Polzin, A. N. Jansen, G. K. Krumdick, and D. L. Wood, "Impact of secondary particle size and two-layer architectures on the high-rate performance of thick electrodes in lithium-ion battery pouch cells." *Journal of Power Sources*, **515**, 230429 (2021).
22. C. Cheng, R. Drummond, S. R. Duncan, and P. S. Grant, "Combining composition graded positive and negative electrodes for higher performance Li-ion batteries." *Journal of Power Sources*, **448**, 227376 (2020).
23. C. Cheng, R. Drummond, S. R. Duncan, and P. S. Grant, "Extending the energy-power balance of li-ion batteries using graded electrodes with precise spatial control of local composition." *Journal of Power Sources*, **542**, 231758 (2022).
24. R. Drummond, C. Cheng, P. S. Grant, and S. R. Duncan, "Modelling the impedance response of graded $LiFePO_4$ cathodes for Li-ion batteries." *J. Electrochem. Soc.*, **169**, 010528 (2022).
25. Y. Zhang, D. Wang, C. Liang, Y. Han, Z. Li, and Y. Huang, "Design of double layer cathode electrode for improving the safety and stability of lithium-ion batteries." *Chemical Engineering Journal*, **495**, 153344 (2024).
26. Y. Yang, G.-R. Xu, A.-P. Tang, J.-c. Zheng, L.-B. Tang, Y.-D. Huang, and H.-Z. Chen, "$Na_3V_2(PO_4)_3$-decorated $Na_3V_2(PO_4)_2F_3$ as a high-rate and cycle-stable cathode material for sodium ion batteries." *RSC Adv.*, **14**, 11862 (2024).

27. R. Diehm, J. Kumberg, C. Dörrer, M. Müller, W. Bauer, P. Scharfer, and W. Schabel, "In situ investigations of simultaneous two-layer slot die coating of component-graded anodes for improved high-energy li-ion batteries." *Energy Technology*, **8**, 1901251 (2020).
28. A. Hoffmann, J. Klemens, S. Raupp, C. Hanske, N. Lawrenz, M. Machate, P. Scharfer, and W. Schabel, "Optimized battery electrodes with primer layers by simultaneous two-layer slot-die coating." *Eur. Phys. J. Spec. Top.*, **234**, 3065 (2024).
29. J. Landesfeind, J. Hattendorff, A. Ehrl, W. A. Wall, and H. A. Gasteiger, "Tortuosity determination of battery electrodes and separators by impedance spectroscopy." *J. Electrochem. Soc.*, **163**, A1373 (2016).
30. J. Landesfeind, D. Pritzl, and H. A. Gasteiger, "An analysis protocol for three-electrode Li-ion battery impedance spectra: part i. analysis of a high-voltage positive electrode." *J. Electrochem. Soc.*, **164**, A1773 (2017).
31. M. Horton et al., "Accelerated data-driven materials science with the materials project." *Nat. Mater.*, **24**, 1522–1532 (2025).
32. A. Jain et al., "Commentary: the materials project: a materials genome approach to accelerating materials innovation." *APL Mater.*, **1**, 011002 (2013).
33. A. Caballero, L. Hernán, J. Morales, L. Sánchez, J. Santos Peña, and M. A. G. Aranda, "Synthesis and characterization of high-temperature hexagonal P2–$Na_{0.6}MnO_2$ and its electrochemical behaviour as cathode in sodium cells." *J. Mater. Chem.*, **12**, 1142 (2002).
34. Z. Jian et al., "Superior electrochemical performance and storage mechanism of $Na_3V_2(PO_4)_3$ cathode for room-temperature sodium-ion batteries." *Adv. Energy Mater.*, **3**, 156 (2013).
35. P. Stüble, C. Müller, J. Klemens, P. Scharfer, W. Schabel, M. Häringer, J. R. Binder, A. Hofmann, and A. Smith, "Enabling long-term cycling stability of $Na_3V_2(PO_4)_3$/C vs. hard carbon full-cells." *Batteries & Supercaps*, **7**, e202300375 (2024).
36. J. Molenda, A. Stokłosa, and D. Than, "Relation between ionic and electronic defects of $Na_{0.7}MnO_2$ bronze and its electrochemical properties." *Solid State Ionics*, **24**, 33 (1987).
37. J. Landesfeind, M. Ebner, A. Eldiven, V. Wood, and H. A. Gasteiger, "Tortuosity of battery electrodes: validation of impedance-derived values and critical comparison with 3D tomography." *J. Electrochem. Soc.*, **165**, A469 (2018).
38. C. Huang, M. Dontigny, K. Zaghib, and P. S. Grant, "Low-tortuosity and graded lithium ion battery cathodes by ice templating." *J. Mater. Chem. A*, **7**, 21421 (2019).
39. A. Shodiev, M. Chouchane, M. Gaberscek, O. Arcelus, J. Xu, H. Oularbi, J. Yu, J. Li, M. Morcrette, and A. A. Franco, "Deconvoluting the benefits of porosity distribution in layered electrodes on the electrochemical performance of li-ion batteries." *Energy Storage Materials*, **47**, 462 (2022).